

A bias-corrected CMIP6 global dataset for dynamical downscaling of future climate, 1979–2100

Zhongfeng Xu (✉ xuzhf@tea.ac.cn)

Institute of Atmospheric Physics, Chinese Academy of Sciences

Ying Han

Institute of Atmospheric Physics, Chinese Academy of Sciences

Chi-Yung Tam

Earth System Science Programme, The Chinese University of Hong Kong <https://orcid.org/0000-0002-5462-6880>

Zong-Liang Yang

Department of Geological Sciences, Jackson School of Geosciences, The University of Texas at Austin
<https://orcid.org/0000-0003-3030-0330>

Congbin Fu

School of Atmospheric Sciences, Nanjing University

Research Article

Keywords: CMIP6, bias correction, dynamical downscaling

Posted Date: April 15th, 2021

DOI: <https://doi.org/10.21203/rs.3.rs-424811/v1>

License:  This work is licensed under a Creative Commons Attribution 4.0 International License.

[Read Full License](#)

A bias-corrected CMIP6 global dataset for dynamical downscaling of future climate, 1979–2100

Authors

Zhongfeng Xu¹, Ying Han¹, Chi-Yung Tam², Zong-Liang Yang³, Congbin Fu⁴

Affiliations

1. RCE-TEA, Institute of Atmospheric Physics, Chinese Academy of Sciences, Beijing, 100029, China

2. Earth System Science Programme, The Chinese University of Hong Kong, Hong Kong, China

3. Department of Geological Sciences, Jackson School of Geosciences, The University of Texas at Austin, Austin, Texas, USA

4. School of Atmospheric Sciences, Nanjing University, 210093, Nanjing, China

corresponding author: Zhongfeng Xu (xuzhf@tea.ac.cn)

Abstract

Dynamical downscaling is an important approach to obtaining fine-scale weather and climate information. However, dynamical downscaling simulations are often degraded by biases in the large-scale forcing itself. Here, we construct a set of bias-corrected global datasets based on 18 models from the Coupled Model Intercomparison Project Phase 6 (CMIP6) and European Centre for Medium-Range Weather Forecasts Reanalysis 5 (ERA5). The bias-corrected data have an ERA5-based mean climate and interannual variance, but with a nonlinear trend from the mean of 18 CMIP6 models. The dataset spans the historical period of 1979–2014 and future scenarios (SSP245 and SSP585) of 2015–2100 with a horizontal resolution of $1.25^\circ \times 1.25^\circ$ and 6-hourly intervals. Our evaluation suggests that the bias-corrected data shows clearly better quality than individual CMIP6 models evaluated in terms of climatological mean, interannual variance and extreme events. The presented dataset will be useful for the dynamical downscaling projections of future climate, atmospheric environment, hydrology, agriculture, wind power, etc.

Background & Summary

Projection of future climate at a finer scale is of great importance to the climate-related studies, such as climate extremes, water resources, agriculture, air quality, and wind power. Common approaches to produce high-resolution projection data include interpolation^{1,2}, statistical downscaling^{3,4}, dynamical downscaling⁵⁻⁸, and hybrid statistical-dynamical downscaling^{9,10}. Compared to the interpolation and statistical downscaling, dynamical downscaling can represent various physical processes as well as their interaction in the climate system, and generate a full set of dynamically consistent high-resolution climate data. Traditional dynamical downscaling (TDD) of future climate involves integrating a regional climate model (RCM) with initial conditions, lateral boundary conditions from a GCM^{6,11}. This TDD approach has been widely used in previous studies^{12,13}. However, GCMs are known to have significant biases, which propagate into RCMs through the lateral boundary and thus degrade the downscaled simulations¹⁴⁻¹⁶.

In recent years, GCM bias corrections are becoming a hot topic in dynamical downscaling studies and many GCM bias correction methods have been developed, e.g., GCM mean bias correction¹⁷⁻¹⁹, GCM mean and variance bias corrections^{16,20}, Quantile-quantile correction²¹, nested bias correction²² and multi-model ensemble (MME) mean-based bias correction²³. Compared to the TDD approach, these bias-correction methods significantly improve downscaling simulations. For example, GCM mean bias correction clearly improved the dynamical downscaling simulation of tropical cyclones over the North Atlantic Ocean^{18,19}. The introduction of variance bias correction further improved the

52 downscaled interannual variability and extreme events¹⁶. MME-based bias correction is
53 expected to generate a more credible downscaling projection of future climate²³.

54 On the other hand, current GCM bias-correction methods also have limitations^{24,25}. For
55 example, Bruyère et al (2014) only corrected GCM mean bias and leave other biases
56 untouched¹⁹. In terms of long-term dynamical downscaling, the variance bias correction may
57 inappropriately modify the GCM trend¹⁶. The quantile-quantile correction cannot retain the
58 intervariable dependencies and introduces an additional bias in the spatial gradient of
59 variables^{21,26}. Note that most bias correction methods are applied to a single model dataset,
60 which suffers greater uncertainty in terms of the projection of future climate. Dai et al. (2017)
61 applied GCM bias correction to MME mean of CMIP5 models. However, they only corrected
62 the GCM mean bias²³.

63 It is well known that the climate projections generated by GCMs are still highly
64 uncertain, especially for precipitation and its extremes²⁷. The source of uncertainties
65 includes the future emission scenarios, internal climate variability, and model uncertainty²⁸.
66 These uncertainties hinder the application of climate projection in impact studies, e.g., the
67 impact of future climate change on water resources and agriculture. Here, we constructed a
68 set of bias-corrected GCM data based on a novel GCM bias correction method. The method
69 takes advantage of the non-linear trend of ensemble mean of 18 Coupled Model
70 Intercomparison Project Phase 6 (CMIP6) models to give a more reliable projection of the
71 long-term climate trend on one hand. On the other hand, we also correct the GCM
72 climatological mean and interannual variance biases based on ERA5. The bias corrections
73 were applied to historical simulations over the period of 1979–2014 and two future
74 scenarios of SSP245 and SSP585 over the period of 2015–2100. This bias-corrected dataset is
75 expected to provide a high-quality large-scale forcing for dynamical downscaling simulation
76 and to improve the reliability of future projections of regional climate and environment.

78 Methods

79 **Data acquisition.** We used the monthly data derived from the CMIP6 historical experiment
80 and future scenarios of SSP245 and SSP585²⁹. The multi-model ensemble mean (MME) of
81 each experiment were calculated using 18 CMIP6 models (Table 1). Previous studies
82 suggested that the MPI-M Earth system models show generally good performance in the
83 simulation of SST and atmospheric circulation among the CMIP5 and CMIP6 models^{30,31}. We,
84 therefore, select the 6-hourly dataset produced by the high-resolution version of the MPI-M
85 earth system model (MPI-M1-2-HR) in CMIP6 to generate weather and interannual variability
86 of the large-scale forcing data. The MPI-ESM1-2-HR is configured with a horizontal grid
87 spacing of 100 km in the atmosphere and 40 km in the ocean³². Compared with its low-
88 resolution counterpart MPI-ESM1.2-LR, MPI-ESM1-2-HR shows improved performance in
89 mid-latitude storm track dynamics, atmospheric blocking, and quasi-biennial oscillation,
90 although the improvement in the mean state relatively modest³²⁻³⁴. The variables used
91 include upper-air temperature, zonal wind, meridional wind, relative humidity, geopotential
92 height, as well as surface pressure, sea level pressure, and sea surface temperature.

93 We also used the ERA5 reanalysis data from 1979 to 2014, which is produced by the
94 European Centre for Medium-Range Weather Forecasts Reanalysis (ECMWF) using 4D-var
95 data assimilation³⁵. Compared to ERA-Interim, ERA5 has a higher horizontal resolution of
96 31km and with more observations assimilated. ERA5 shows considerable improvement in
97 tropospheric temperature, wind, and humidity, but not in the stratosphere with respect to
98 ERA-Interim. Both the ERA5 and CMIP6 data were regridded to a horizontal resolution of 1.25°
99 longitude × 1.25° latitude by bilinear interpolation.

100
101 **GCM bias-correction method.** The bias corrections are applied to 6-hourly data. Each non-
102 leap year contains 1460 data points. For each 6-hour and day of the year, the ERA reanalysis

103 (orange curve in Fig.1) and GCM output (red curve in Fig.1) can be broken down into a long-
 104 term nonlinear trend plus an interannual perturbation term:

$$105 \quad GCM = GCM_{LT} + GCM' \quad (1)$$

$$106 \quad ERA = ERA_{LT} + ERA' \quad (2)$$

107 The nonlinear trend was calculated with the EEMD method³⁶. Unlike the previous
 108 decomposition that broke the GCM into a climatological mean plus a perturbation term as in
 109 previous studies^{16,17}, our decomposition excludes the long-term trend in the perturbation
 110 term, which can avoid inappropriate modification on the long-term trend during the variance
 111 bias correction. Note that the GCM may also overestimate or underestimate the amplitude
 112 of interannual variations. This bias can be measured by the ratio of GCM variance to
 113 reanalysis variance. We assume that the variance bias remains the same from the historical
 114 to a future period. Thus, we can correct the variance bias by multiplying the perturbation
 115 term by a scaling factor, r_s :

$$116 \quad GCM_v = GCM_{LT} + GCM' \times r_s \quad (3)$$

117 where $r_s = \sigma_{ERA} / \sigma_{GCM}$ is the ratio of the standard deviation of detrended reanalysis to that
 118 of detrended GCM over the historical period. As the standard deviations are computed using
 119 detrended data, we, therefore, adjust the variance of interannual and interdecadal variation
 120 and remain the nonlinear trend unchanged (blue curve in Fig.1). Otherwise, the long-term
 121 trend may also be changed inappropriately if we use the standard deviation of the original
 122 time series to adjust the variance³⁸.

123 It is known that single-GCM projections of long-term trend give greater uncertainty
 124 compared to the MME mean. To reduce the certainty of future projection, we replace the
 125 long-term nonlinear trend derived from the single GCM with that derived from MME in Eq.
 126 (3). Thus the new GCM data (green curve in Fig.1) can be rewritten as:

$$127 \quad GCM_{vt} = MME_{LT} + GCM' \times r_s \quad (4)$$

128 MME_{LT} is the nonlinear trend of MME computed with EEMD over the historical-future
 129 period. Eq. (4) can be further rearranged according to:

$$130 \quad GCM_{vt} = MME_{LT} + (\overline{MME_{LT|H}} - \overline{ERA_{LT|H}}) - (\overline{MME_{LT|H}} - \overline{ERA_{LT|H}}) + GCM' \times r_s \quad (5)$$

131 The subscript H represents the historical period (1979–2014), while the overbar indicates the
 132 climatological mean. $(\overline{MME_{LT|H}} - \overline{ERA_{LT|H}})$ is the mean bias of GCM long-term trend
 133 relative to that of the reanalysis over the historical period, which can be removed to correct
 134 the GCM mean bias. Further bias-corrected data can be constructed as follows:

$$135 \quad GCM_{vtm} = MME_{LT} - (\overline{MME_{LT|H}} - \overline{ERA_{LT|H}}) + GCM' \times r_s \quad (6)$$

$$136 \quad = \overline{ERA_{LT|H}} + (\overline{MME_{LT}} - \overline{MME_{LT|H}}) + GCM' \times r_s$$

137 Thus, the bias-corrected 6-hourly GCM data over the future period have a base climate
 138 provided by reanalysis data over the historical period, with the change in future climate
 139 relative to the historical climatology generated by MME, and future bias-corrected weather
 140 and climate variability derived from a single GCM. Eq. (6) is the final equation that corrects
 141 GCM mean and variance biases after replacing the single GCM nonlinear trend with the MME
 142 nonlinear trend (black curve in Fig.1).

143 The EEMD method used to compute the nonlinear trend is very time-consuming if we
 144 apply EEMD to process global 6-hourly 3-D data sets over multiple decades. To save
 145 computing time, we assume that the nonlinear trends remain the same for each 6-
 146 hourly/daily value of variables within the same month. Thus, the climatological mean of the
 147 detrended data, $\frac{1}{N} \sum_{i=1}^N (GCM - GCM_{LT})$, is not exactly equal to zero because the GCM and
 148 GCM_{LT} are derived from 6-hourly data and monthly data, respectively. Before correcting the
 149 variance biases, we compute the anomaly of detrended GCM data at each 6-hourly
 150 interval/day of the year:

$$149 \quad GCM' = (GCM - GCM_{LT}) - \frac{1}{N} \sum_{i=1}^N (GCM - GCM_{LT}) \quad (7)$$

150 The first term on the right-hand side of Eq. (7) represents the detrended GCM data. The
 151 standard deviation of each 6-hour and day of the year is calculated across 36 years from

152 1979 to 2014. Note that extreme events, e.g., tropical cyclone, can strongly affect the
153 interannual standard deviations of many variables, such as the sea level pressure,
154 geopotential height, and wind. As tropical cyclones occur in different locations in the CMIP6
155 model and reanalysis, the ratio of standard deviation in the grid cells with tropical cyclones
156 would be unrealistically different from its surrounding regions. To remove the unrealistic
157 ratios of standard deviation, we first calculate the original standard deviation with all 36
158 years of data and then recalculate the standard deviation after removing the years with
159 anomalies greater than 3 times the original standard deviation.

160

161 **Evaluation methods.** To comprehensively compare the performance of bias-corrected GCM
162 data with other CMIP6 models, we computed the commonly used statistics, such as mean
163 error (ME), correlation coefficient (CORR), standard deviation (SD), and root-mean-square
164 difference (RMSD). To assess the overall performance of climate model in simulating
165 multiple fields, we also employed a multivariable integrated skill score (MISS). MISS is
166 defined based on the vector fields statistics and can summarize the model overall
167 performance in simulating multiple fields³⁸⁻⁴⁰. Model performance improves monotonically
168 with an increase in MISS. MISS approaches 1 when the modeled multiple fields are close to
169 observed values. Thus, MISS can be used to rank the performance of various CMIP6 models
170 in simulating multiple fields.

171

172 **Data Records**

173 The dataset includes 3 surface variables and 8 upper-air variables for three sets of bias-
174 corrected CMIP6 data, the historical data from 1979 to 2014, SSP245 and SSP585 from 2015
175 to 2100 (Table 2). We provide the data at a horizontal resolution of 1.25° longitude \times 1.25°
176 and 6 hourly interval. The upper-air variables consist of 14 pressure levels, i.e., 1000, 925,
177 850, 700, 600, 500, 400, 300, 250, 200, 150, 100, 70, and 50 hPa. All the bias-corrected data
178 was stored in self-describing NetCDF format (<http://doi.org/10.5065/D6H70CW6>). The
179 NetCDF files are named as “atm_experiment_yyyy_mm.nc4”, where “experiment” denotes
180 the historical, SSP245, or SSP585 experiments. “yyyy” and “mm” denote the year and month
181 of the data, respectively. Each file includes all 6-hourly data for one month of a year. The
182 complete data set is ~1.9 TB in size. All data are freely available at the China Science Data
183 Bank⁴¹.

184

185 **Technical Validation**

186 **Time series.** To validate the bias-correction GCM data, we compared the 600-hPa air
187 temperature in Northwest Pacific derived from the original GCM, bias-corrected GCM
188 (GCMbc), and ERA5 in Fig. 2. The original GCM data overestimate air temperature by 1.37°C
189 over the historical period (1979–2014) relative to ERA5 (Fig. 2a). The mean bias is
190 completely removed in the bias-corrected GCM data. Compared to ERA5, the original GCM
191 underestimates the amplitude of interannual variability characterized by a standard
192 deviation of 0.54 in GCM against 0.85 in ERA5. The variance bias is also removed in the bias-
193 corrected GCM data. Besides, the GCM and GCMbc show different long-term trends because
194 the GCMbc follows the non-linear trend of MME of 18 CMIP5 models. Note that the bias
195 correction method proposed in this study affects the GCM mean, variance, and non-linear
196 trend but does not affect the phase of interannual variation. GCMbc inherits the phase of
197 interannual variation from the selected GCM, i.e., MPI-ESM1-2-HR.

198 The frequency distribution of 600-hPa air temperature indicates that the GCM
199 significantly overestimates the high-temperature events but underestimate the low-
200 temperature ones relative to ERA5 (Fig. 2b). In contrast, the bias-corrected GCM, i.e. GCMbc,
201 shows a frequency distribution very similar to that from ERA5. This indicates that the bias
202 correction methods can also significantly improve the GCM extreme events characteristics.

203 Under the SSP585 scenario (Fig. 2c), the temperature is a non-stationary time series in
204 association with global warming. Consequently, the frequency distribution of temperature
205 does not follow a normal distribution. The change in the frequency distribution during the
206 future period is similar to that during the historical periods characterized by a shift towards a
207 colder climate and an enhanced variance.

208

209 **Climatological mean.** The climatology of the bias-corrected GCM data and 18 CMIP6 models
210 are assessed against ERA5 with multiple statistics, e.g., mean error (ME), spatial standard
211 deviation (SD), and correlation coefficient (CORR) for multiple variables. All statistics were
212 normalized by dividing the observed standard deviation of the corresponding variable to
213 facilitate the intercomparison between different variables. The results suggest that CMIP6
214 models show greater ME of 200-hPa air temperature and 850-hPa relative humidity (Fig. 3).
215 Most CMIP6 models underestimate the 200-hPa air temperature, as indicated by negative
216 MEs ranging from 0.3 to 2 times of standard deviation. On the other hand, 12 out of 18
217 CMIP6 models significantly overestimate the 850-hPa relative humidity by ~ 0.3 – 2 standard
218 deviation. CMIP6 models also show relatively poor performance in the spatial pattern of 200-
219 hPa air temperature and 850-hPa relative humidity characterized by smaller CORR than
220 other variables. For the climatological mean of multiple variables, EC-Earth3, EC-Earth3-Veg,
221 AWI-CM-1-1-MR, GFDL-CM4, and MPI-ESM1-2-HR ranks the top 5 out of 18 CMIP6 models.
222 The mean errors in the bias-corrected GCM data (MPI-ESM1-2-HR_bc) are completely
223 removed. In another word, the climatology of the bias-corrected GCM is the same as those
224 of ERA5 during the historical period.

225

226 **Extreme values.** The extreme values in the large-scale forcing data will likely affect the RCM
227 simulations through the lateral and underlying boundary conditions. To examine the impacts
228 of bias corrections on extreme values, we calculate the 95 percentile of daily SST and 850-
229 hPa wind speed during July of 1979–2014 (Fig. 4). The GCM (i.e., MPI-ESM1-2-HR)
230 overestimates the high SST extreme over the Intertropical Pacific convergence zone and
231 South Pacific convergence zone by 1 – 2 °C but underestimate the high SST extreme by
232 approximately -2 °C in the central North Pacific and Atlantic Oceans (Fig. 4c). In the bias-
233 corrected GCM data, the bias of high SST extreme is generally less than 0.5 °C except in the
234 eastern coast of the central Pacific where there is a negative bias of about -1 °C (Fig. 4e).
235 Wind is another key variable that transfers energy and moisture into RCM through the LBC.
236 The RCM simulation is strongly affected by the wind circulation, especially that with an
237 inward component^{42,43}. The GCM significantly overestimates the 850-hPa wind speed over
238 East Asia, South Europe–West Asia, and western North America by approximately 3 – 5 m s⁻¹
239 but underestimates that over most parts of the Pacific Ocean (Fig. 4d). These biases are
240 significantly reduced in the bias-corrected GCM data with typical wind speed bias less than 1
241 m s⁻¹. Note that we did not directly correct the biases of extreme values per se. However,
242 the bias correction to mean and variance biases will in turn improve the extreme values.

243

244 **Long-term nonlinear trends.** Figure 5 illustrates the non-linear trends of January-mean 850-
245 hPa air temperature from 2015 to 2100. To facilitate intercomparison of various models,
246 each of the non-linear trends subtracts its value in the year 2015. Under the SSP585 scenario,
247 CMIP6 models show a 3 – 6.8 °C increase in the non-linear trend of global mean 850-hPa air
248 temperature across 18 CMIP6 models by the end of the 21st century. Clearly, CMIP6 models
249 still show a large uncertainty in the projection of global mean 850-hPa air temperature.
250 Same as MME, the bias-corrected GCM shows a 4.2 °C increase in 850-hPa air temperature
251 against the 3.5 °C increase in the MPI-ESM1-2-HR model by the end of the 21st century.

252 To more comprehensively compare the difference in non-linear trend among various
253 CMIP6 models, we computed the cRMSD of the non-linear trend of each model relative to
254 that of MME (Fig. 5b). A smaller cRMSD indicates that the non-linear trend of the

255 corresponding model is closer to that of MME. Compared to all of the CMIP6 models
 256 evaluated, the bias-corrected GCM shows the minimum cRMSE for all variables. The cRMSEs
 257 are reduced by approximately 70–90% after bias corrections. Note that the non-linear trend
 258 of bias-corrected GCM should be the same as that of MME for each 6 hours and day of the
 259 year. However, the non-linear trends in figure 5b were computed using monthly mean data
 260 rather than the 6-hourly data. The anomalous time series are multiplied by different scaling
 261 factors on different days during the variance bias correction. Thus, the monthly mean of the
 262 bias-corrected data will show non-linear trends slightly different from those of MME.

263
 264 **Intervariable dependency.** It was argued that the independent bias correction to individual
 265 variables can disturb the intervariable dependency, which may degrade the RCM simulation
 266 to a certain extent^{26,44}. To examine the impacts of bias correction on the intervariable
 267 dependency, we computed the geostrophic wind based on the geostrophic balance

$$u_g = -\frac{1}{f} \left(\frac{\partial gz}{\partial y} \right)_p$$

$$v_g = -\frac{1}{f} \left(\frac{\partial gz}{\partial x} \right)_p$$

268 where u_g and v_g are the zonal and meridional components of geostrophic wind, respectively,
 269 g the acceleration of gravity, z the geopotential height, f the Coriolis parameter. The
 270 geostrophic wind is a result of the balance between the horizontal pressure gradient and
 271 Coriolis force. The ageostrophic wind, i.e., geostrophic wind deviation, is defined by the
 272 vector difference between the real wind and the geostrophic wind:

$$u_a = u - u_g$$

$$v_a = v - v_g$$

273 The ratio of ageostrophic wind speed to the real wind speed is calculated by

$$R = \frac{\sqrt{u_a^2 + v_a^2}}{\sqrt{u^2 + v^2}}$$

274 R can also be interpreted as the percentage of geostrophic wind deviation to real wind speed.
 275 In general, R is expected to increase if the bias correction significantly disturbs the balance
 276 between the horizontal wind and geopotential height. Thus, the difference of R between
 277 GCM and GCMbc can indicate the impact of bias correction on the dependency between
 278 wind and geopotential height. For comparison, we also calculated R for the ERA5 data.

279 The vertical profile of global mean R in GCMbc is very close to that in GCM and both
 280 show greater R than the ERA5 (Fig. 6). In the low latitudes, the bias correction leads to a
 281 decrease in geostrophic deviation because the GCM biases are corrected based on ERA5 and
 282 the geostrophic deviation is smaller in ERA5 than GCM (Fig. 6b). In the mid to high latitudes
 283 Northern Hemisphere, bias correction causes moderate but significant increases in R (less
 284 than 0.02). In East Asia, the comparison of GCMbc with GCM indicates that bias correction
 285 also leads to significant increases in R. However the difference of R between GCMbc and
 286 ERA5 are less significant below 300 hPa (Fig. 6e). In the Northwest Pacific, bias correction has
 287 minor impacts on the intervariable dependency characterized by a less significant difference
 288 of R between the GCMbc and GCM (ERA5). Overall, bias correction does disturb the
 289 intervariable dependency to a certain extent. The geostrophic wind deviation can increase by
 290 approximately 20% in the mid and high latitudes of the Northern Hemisphere. Globally, only
 291 10% of the area shows significant differences in R between the GCM and GCMbc. The
 292 disturbance of intervariable dependency induced by bias correction may affect the
 293 dynamical downscaling simulation to a certain extent. However, the impacts are expected to
 294 be small for a long-term simulation since the imbalance only appears in the initial and lateral
 295 boundary conditions of RCM²⁰. In contrast, the bias correction-induced imbalance in GCM
 296 could significantly affect RCM simulation if nudging was employed during the integration of
 297 RCM. In this case, one may consider reducing the strength of nudging²⁰.

298

299 **Usage Notes**

300 The China Science Data Bank provides the open-access data presented in this article, with a
301 DOI (<http://www.dx.doi.org/10.11922/sciencedb.00487>). The NetCDF data was compressed
302 to save space. Users should use two attributes, `scale_factor` and `add_offset`, to unpack the
303 variables. We provide a FORTRAN code to convert these compressed NetCDF files to WRF
304 intermediate files (supplementary file). In addition to FORTRAN, a lot of software are
305 available to manipulating or displaying NetCDF data, e.g., CDO, NCO, NCL, Python, Ncview,
306 GrADS. More software can be found at
307 <https://www.unidata.ucar.edu/software/netcdf/software.html>. The data provided here can
308 be used to generate the lateral and underlying condition of RCM.

309 Besides, RCMs also need the surface air temperature, soil temperature, soil moisture as
310 initial conditions. In terms of long-term climate projection, the bias correction for the initial
311 condition would be less necessary. As the spin-up time of atmospheric variables is generally
312 less than a month. The deep soil temperature and moisture do need a much longer time to
313 spin up. Users can generate these data through an offline simulation of the land surface
314 model driven by atmospheric forcing.

315 **Code Availability**

316 The code used to produce the bias-corrected global CMIP6 data is publicly available
317 (supplementary file). The code consists of an NCL (version 6.6.2) script to compute non-linear
318 trends and a few CDO (version 1.7.0) scripts to regrid data and correct CMIP6 data biases.

319

320 **Acknowledgements**

321 We acknowledge the World Climate Research Programme' s Working Group on Coupled
322 Modelling, which is responsible for CMIP, and we thank the climate modeling groups for
323 producing and making available their model output. ERA5 Reanalysis data was provided by
324 the European Centre for Medium-Range Weather Forecasts at the website
325 <https://www.ecmwf.int/en/forecasts/datasets/reanalysis-datasets/era5>. ZX is supported
326 jointly by the National Key Research and Development Program of China (2018YFA0606004)
327 and National Natural Science Foundation of China (42075170). YH is supported jointly by the
328 National Key Research and Development Program of China (2017YFA0603803) and National
329 Science Foundation of China (41675105). CYT is supported by the Chinese University Direct
330 Grant (No. 4053331).

331

332 **Author contributions**

333 ZX developed the GCM bias correction method and processed the CMIP6 data. ZX and YH
334 perform the validation of bias corrected data against reanalysis data. All co-authors
335 contributed to writing and commented on the manuscript.

336

337 **Competing interests**

338 The authors declare that they have no conflict of interest.

339

340

341

342
343

Figures

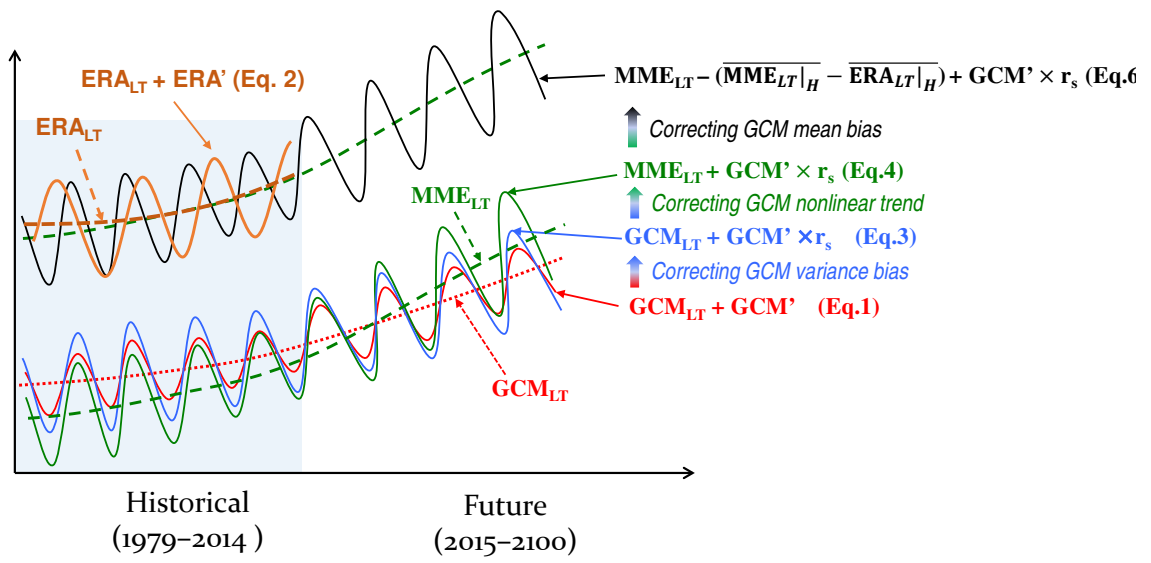


Fig. 1 Schematic chart for the process of GCM bias corrections

344

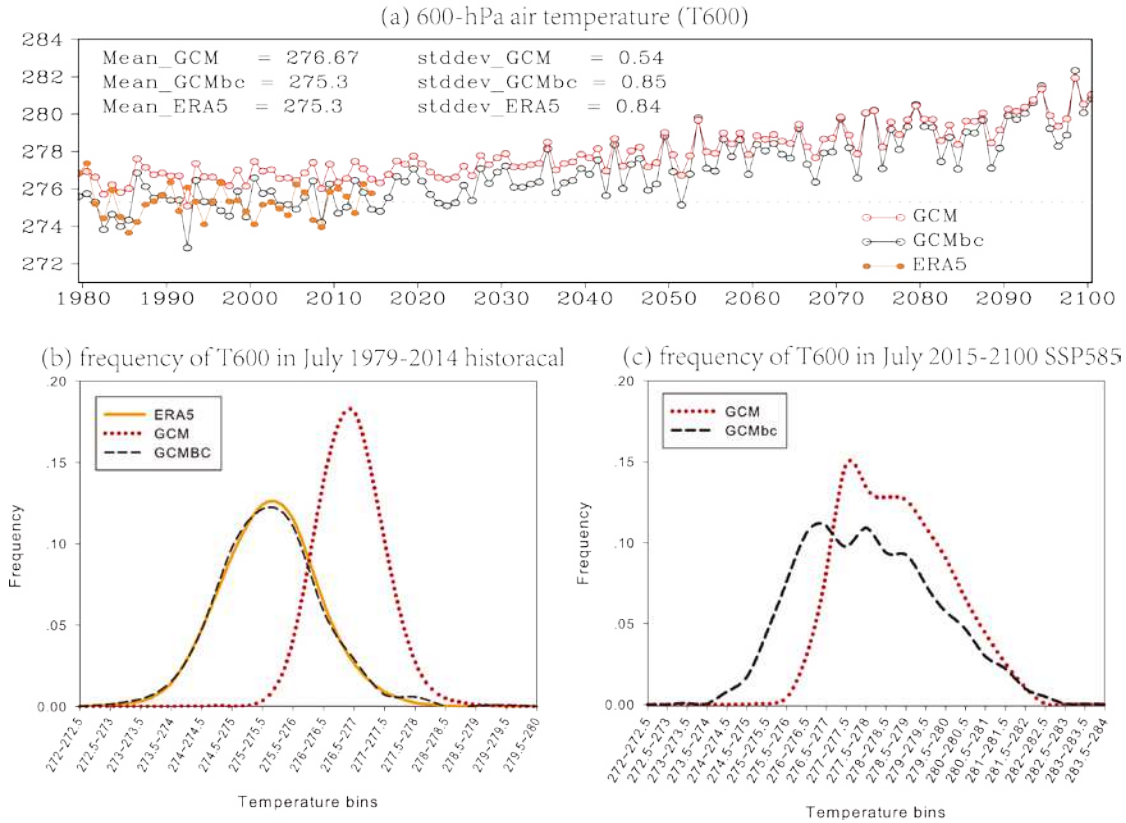


Fig. 2 Comparison of the original and bias-corrected data GCM data (GCMbc) with ERA5 during the historical (1979–2014) period and SSP585 scenarios (2015–2100). (a) 600-hPa air temperature (T600) in Northwest Pacific (10°N, 135°E) at 00 UTC July 15 from 1979 to 2100. The 36-yr averaged (1979–2014) value and temporal standard deviation for each data are shown on the upper-left of (a). The frequency distribution of T600 in July during the period of (a) 1979–2014 and (b) 2015–2100 under SSP585 scenarios. The frequency (in percentage) is computed based on the instantaneous data at 00 UTC in July. There are 1116 days (31 day × 36 year) and 2666 days (31 day × 86 year) are included in the statistics for the historical and future periods, respectively.

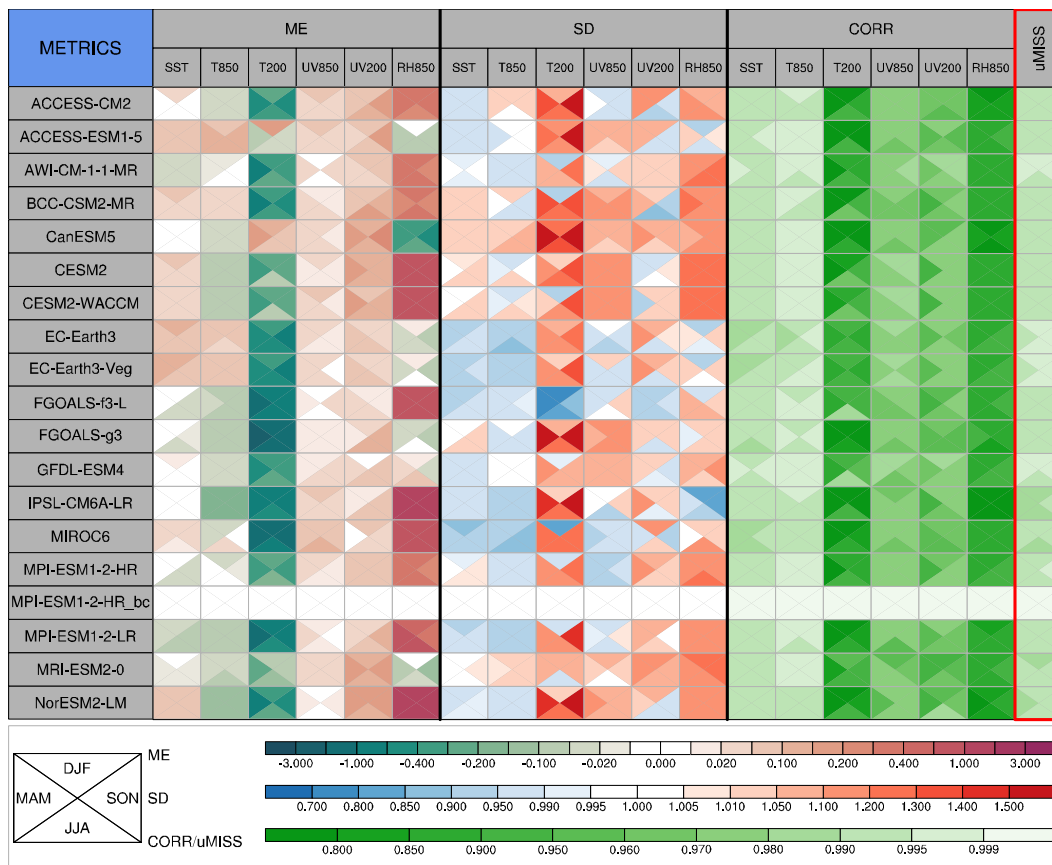


Fig. 3 Statistical metrics that measure the performance of CMIP6 models in simulating climatological mean (1979 – 2014) of multiple variables. SST: sea surface temperature, T850: 850-hPa air temperature, UV850: 850-hPa vector wind, RH850: 850-hPa relative humidity, T200: 200-hPa air temperature, UV200: 200-hPa vector wind in the global. ME, SD, and CORR are the mean error, spatial standard deviation, and correlation coefficient of the climatological mean field, respectively. uMISS is the uncentered multivariable integrated skill score that summarizes the overall performance of a model in simulating multiple variables. All statistics are normalized by dividing the observed standard deviation of the corresponding variable. All models are evaluated against ERA5. Lighter color represents better model performance. MPI-ESM1-2-HR_bc is the bias-corrected GCM data.

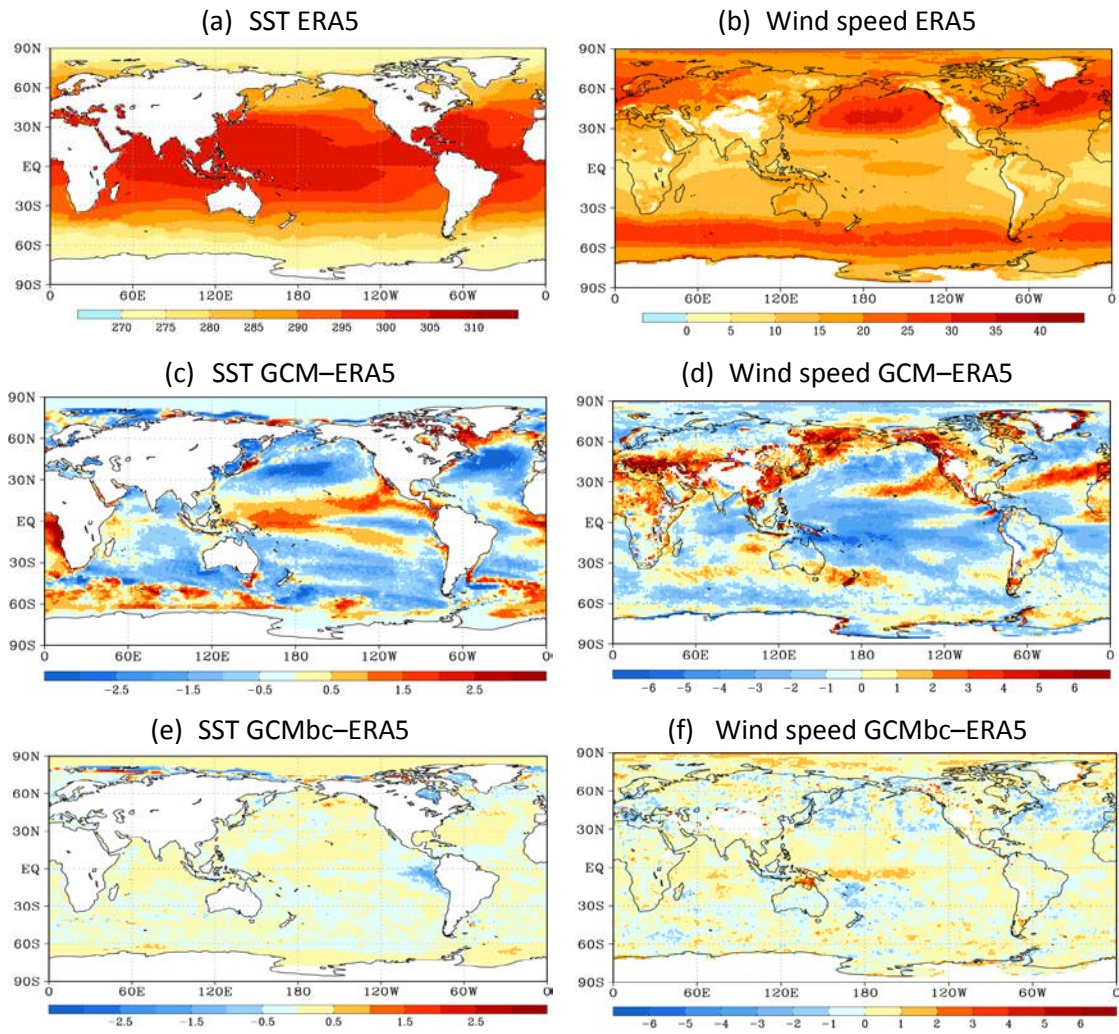


Fig. 4 Comparison of the 95th percentile of daily SST ($^{\circ}\text{C}$) and 850-hPa wind speed wind (m s^{-1}) during July of 1979–2014 against ERA5. (a, b) ERA5, (c-f) difference between GCM (GCMbc) and ERA5.

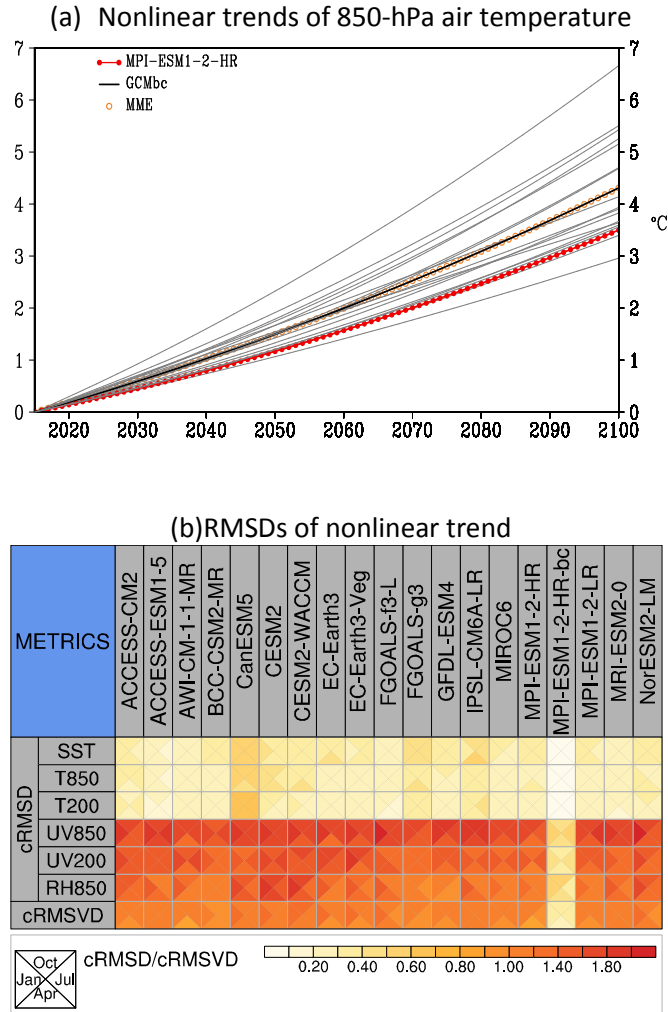


Fig. 5 Comparison of Nonlinear trend of various CMIP6 data against multi-model ensemble mean (MME) in July from 2015 to 2100 under SSP585 scenario. (a) Global 850-hPa air temperature. The orange open circle, red solid circles, and the thick black line represent the MME, MPI-ESM1-2-HR model the bias-corrected MPI-ESM1-2-HR model, respectively. The grey line indicates the other 17 CMIP6 models. The value of the non-linear trend in the year 2015 was subtracted from the original non-linear trend. (b) root-mean-square differences of the non-linear trends between the individual CMIP6 model and the MME. As in Fig. 3 the cRMSDs are also normalized by dividing the observed standard deviation of the corresponding variable. The cRMSVD represents the overall RMSD of all variables. The triangles in each grid cell represent the statistic in January, April, July, and October, respectively.

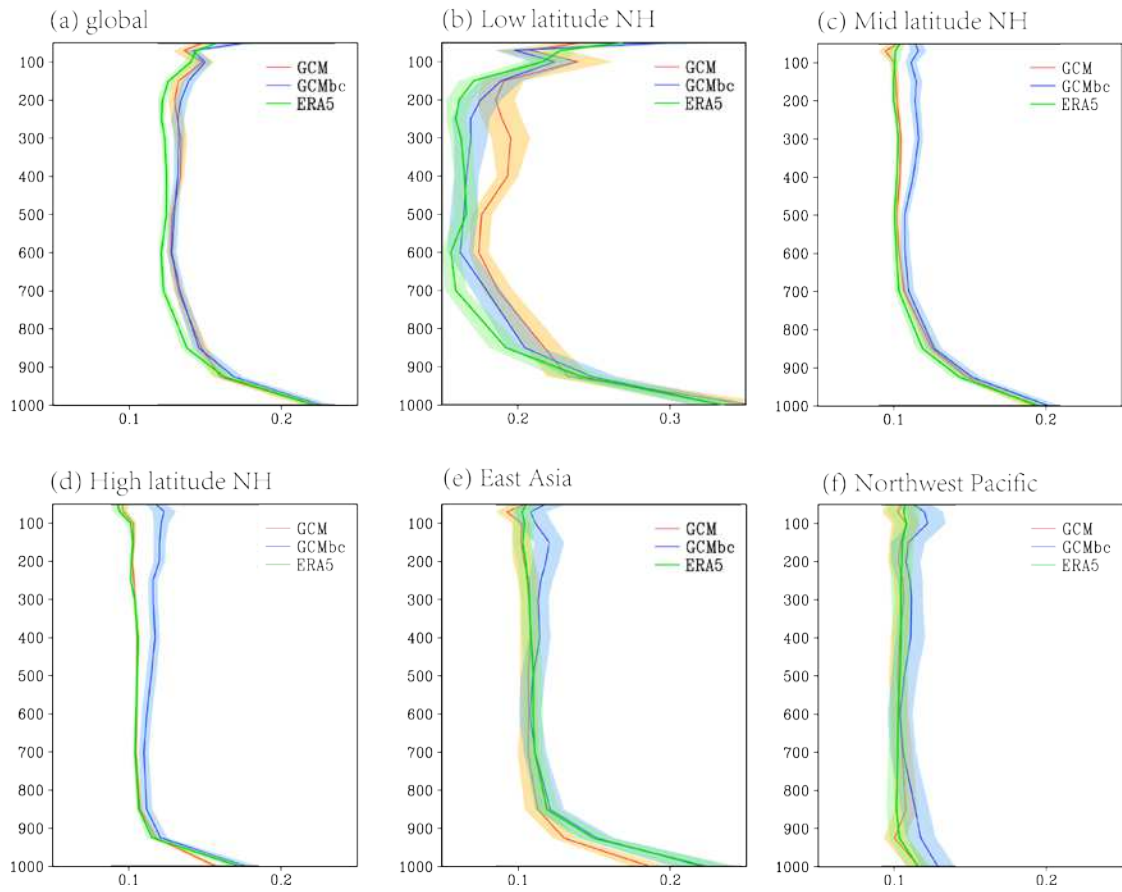


Fig. 6 The ratio (R) of ageostrophic wind speed to the real wind speed averaged over various regions in July 2014. The shading shows the one standard deviation. The ageostrophic wind and real wind are calculated using 6-hourly data in July 2014. The area-mean R is computed in mid (20° – 50° N, 0 – 358.75° E) and high latitudes (50 – 90° N, 0 – 358.75° E) of Northern Hemisphere, East Asia (10° – 55° N, 105° – 140° E), and Northwest Pacific (10° – 40° N, 135° E– 180°). The grid cells with wind speed less than 2 m s^{-1} were excluded from the statistics.

353

354 **Figure Legends**

355

356 Fig. 2 Schematic chart for the process of GCM bias corrections

357

358 Fig. 2 Comparison of the original and bias-corrected data GCM data (GCMbc) with ERA5
359 during the historical (1979–2014) period and SSP585 scenarios (2015–2100). (a) 600-hPa air
360 temperature (T600) in Northwest Pacific (10°N, 135°E) at 00 UTC July 15 from 1979 to 2100.
361 The 36-yr averaged (1979–2014) value and temporal standard deviation for each data are
362 shown on the upper-left of (a). The frequency distribution of T600 in July during the period
363 of (a) 1979–2014 and (b) 2015–2100 under SSP585 scenarios. The frequency (in percentage)
364 is computed based on the instantaneous data at 00 UTC in July. There are 1116 days (31 day
365 × 36 year) and 2666 days (31 day × 86 year) are included in the statistics for the historical
366 and future periods, respectively.

367

368 Fig. 3 Statistical metrics that measure the performance of CMIP6 models in simulating
369 climatological mean (1979 – 2014) of multiple variables. SST: sea surface temperature, T850:
370 850-hPa air temperature, UV850: 850-hPa vector wind, RH850: 850-hPa relative humidity,
371 T200: 200-hPa air temperature, UV200: 200-hPa vector wind in the global. ME, SD, and CORR
372 are the mean error, spatial standard deviation, and correlation coefficient of the
373 climatological mean field, respectively. uMISS is the uncentered multivariable integrated skill
374 score that summarizes the overall performance of a model in simulating multiple variables.
375 All statistics are normalized by dividing the observed standard deviation of the
376 corresponding variable. All models are evaluated against ERA5. Lighter color represents
377 better model performance. MPI-ESM1-2-HR_bc is the bias-corrected GCM data.

378

379 Fig. 4 Comparison of the 95th percentile of daily SST (°C) and 850-hPa wind speed wind (m s^{-1})
380 during July of 1979–2014 against ERA5. (a, b) ERA5, (c-f) difference between GCM (GCMbc)
381 and ERA5.

382

383 Fig. 5 Comparison of Nonlinear trend of various CMIP6 data against multi-model ensemble
384 mean (MME) in July from 2015 to 2100 under SSP585 scenario. (a) Global 850-hPa air
385 temperature. The orange open circle, red solid circles, and the thick black line represent the
386 MME, MPI-ESM1-2-HR model the bias-corrected MPI-ESM1-2-HR model, respectively. The
387 grey line indicates the other 17 CMIP6 models. The value of the non-linear trend in the year
388 2015 was subtracted from the original non-linear trend. (b) root-mean-square differences of
389 the non-linear trends between the individual CMIP6 model and the MME. As in Fig. 3 the
390 cRMSDs are also normalized by dividing the observed standard deviation of the
391 corresponding variable. The cRMSVD represents the overall RMSD of all variables. The
392 triangles in each grid cell represent the statistic in January, April, July, and October,
393 respectively.

394

395 Fig. 6 The ratio (R) of ageostrophic wind speed to the real wind speed averaged over various
396 regions in July 2014. The shading shows the one standard deviation. The ageostrophic wind
397 and real wind are calculated using 6-hourly data in July 2014. The area-mean R is computed
398 in mid (20°–50°N, 0–358.75°E) and high latitudes (50–90°N, 0–358.75°E) of Northern
399 Hemisphere, East Asia (10°–55°N, 105°–140°E), and Northwest Pacific (10°–40°N, 135°E–
400 180°). The grid cells with wind speed less than 2 m s^{-1} were excluded from the statistics.

401

402

403 **Tables**

404

405 Table 1. CMIP6 models used in this study

No.	Model	Institution	Grid spacing
1	ACCESS-CM2	Commonwealth Scientific and Industrial Research Organisation, and Australian Research Council Centre of Excellence for Climate System Science (Australia)	$\sim 1.875^\circ \times 1.25^\circ$
2	ACCESS-ESM1-5	Commonwealth Scientific and Industrial Research Organisation (Australia)	$\sim 1.875^\circ \times 1.25^\circ$
3	CanESM5	Canadian Centre for Climate Modelling and Analysis, Environment and Climate Change (Canada)	$\sim 2.81^\circ \times 2.81^\circ$
4	BCC-CSM2-MR	Beijing Climate Center (China)	$\sim 1.125^\circ \times 1.125^\circ$
5	FGOALS-f3-L	Institute of Atmospheric Physics, Chinese Academy of Sciences (China)	$\sim 1.25^\circ \times 1^\circ$
6	FGOALS-g3	Institute of Atmospheric Physics, Chinese Academy of Sciences (China)	$\sim 2^\circ \times 2.25^\circ$
7	EC-Earth3	European community (including multiple institutes from Spain, Italy, Denmark, Germany, Ireland, Portugal, Netherlands, Sweden, Norway, UK, Belgium, and Finland)	$\sim 0.70^\circ \times 0.70^\circ$
8	EC-Earth3-Veg	European community	$\sim 0.70^\circ \times 0.70^\circ$
9	IPSL-CM6A-LR	Institute Pierre Simon Laplace (France)	$\sim 2.5^\circ \times 1.27^\circ$
10	AWI-CM-1-1-MR	Alfred Wegener Institute, Helmholtz Centre for Polar and Marine Research (Germany)	$\sim 0.94^\circ \times 0.94^\circ$
11	MPI-ESM1-2-HR	Max Planck Institute for Meteorology, and Deutsches Klimarechenzentrum (Germany)	$\sim 0.94^\circ \times 0.94^\circ$
12	MPI-ESM1-2-LR	Max Planck Institute for Meteorology, and Alfred Wegener Institute, Helmholtz Centre for Polar and Marine Research (Germany)	$\sim 1.875^\circ \times 1.875^\circ$
13	MIROC6	Japan Agency for Marine-Earth Science and Technology, Atmosphere and Ocean Research Institute, National Institute for Environmental Studies, and RIKEN Center for Computational Science (Japan)	$\sim 1.41^\circ \times 1.41^\circ$
14	MRI-ESM2-0	Meteorological Research Institute (Japan)	$\sim 1.125^\circ \times 1.125^\circ$
15	NorESM2-LM	Center for International Climate and Environmental Research, Norwegian Meteorological Institute, Nansen Environmental and Remote Sensing Center, NERSC, Norwegian Institute for Air Research, University of Bergen, University of Oslo, Uni Research (Norway)	$\sim 2.5^\circ \times 1.89^\circ$
16	CESM2	National Center for Atmospheric Research, Climate and Global Dynamics Laboratory (USA)	$\sim 1.25^\circ \times 0.94^\circ$
17	CESM2-WACCM	National Center for Atmospheric Research, Climate and Global Dynamics Laboratory (USA)	$\sim 1.25^\circ \times 0.94^\circ$
18	GFDL-ESM4	Geophysical Fluid Dynamics Laboratory (USA)	

406

407

408 Table 2 The bias-corrected variables

Variables	Acronym	Vertical levels	Historical 1979–2014	SSP245 2015–2100	SSP585 2015–2100
Sea surface temperature	tos	1	√	√	√
Sea level pressure	psl	1	√	√	√
Surface pressure	ps	1	√	√	√
Air temperature	ta	14	√	√	√
Zonal wind	ua	14	√	√	√
Meridional wind	va	14	√	√	√
relative humidity	hur	14	√	√	√
Geopotential height	zg	14	√	√	√

409

410

411 **References**

- 412 1. Marchi, M., Castellanos-Acuña, D., Hamann, A., Wang, T. Ray D., & Menzel, A. ClimateEU,
413 scale-free climate normals, historical time series, and future projections for Europe.
414 *Scientific Data*, **7**, 428. <https://doi.org/10.1038/s41597-020-00763-0> (2020).
- 415 2. Navarro-Racines, C., Tarapues, J., Thornton, P., Jarvis A. & Ramirez-Villegas, J. High-
416 resolution and bias-corrected CMIP5 projections for climate change impact assessments.
417 *Scientific Data* **7**, <https://doi.org/10.1038/s41597-019-0343-8> (2020).
- 418 3. Wilby, R. L. et al. Statistical downscaling of general circulation model output: A
419 comparison of methods. *Water Resources Research*, **34(11)**, 2995–3008 (1998).
- 420 4. Fan, L., Chen, D., Fu, C. & Yan, Z. Statistical downscaling of summer temperature extremes
421 in northern China. *Adv. Atmos. Sci.* **30(4)**, 1085–1095, doi: 10.1007/s00376-012-2057-0
422 (2013).
- 423 5. Giorgi, F., Brodeur, C. S. & Bates, G. T. Regional climate change scenarios over the United
424 States produced with a nested regional climate model. *J. Climate*, **7**, 357–399, (1994).
- 425 6. Giorgi, F., Jones, G. & Asrar, G. R. Addressing climate information needs at the regional
426 level: The CORDEX framework, *WMO Bull*, **58(3)**, 175–183 (2009).
- 427 7. Fu C. et al. Regional Climate Model Intercomparison Project for Asia. *Bull. Amer. Meteorol.*
428 *Soc.* **86**, 257–266 (2005).
- 429 8. Gutowski, W.J. The ongoing need for high-resolution regional climate models: Process
430 understanding and stakeholder information. *Bull. Amer. Meteorol. Soc.* **101(5)**, E664–
431 E683; DOI: <https://doi.org/10.1175/BAMS-D-19-0113.1> (2020).
- 432 9. Walton, D., Sun, F., Hall, A. & Capps, C. A hybrid dynamical–statistical downscaling
433 technique. Part I: Development and validation of the technique. *J. Climate*, **28**, 4597–4617
434 (2015).
- 435 10. Sun, F, Walton, D., & Hall, A. A Hybrid Dynamical-Statistical Downscaling Technique, Part
436 II: End-of-Century Warming Projections Predict a New Climate State in the Los Angeles
437 Region. *J. Climate*, **28**, 4618–4636 (2015).
- 438 11. Giorgi, F. & Mearns, L. O. Introduction to special section: Regional climate modeling
439 revisited. *J. Geophys. Res.* **104**, 6335–6352, doi:10.1029/98JD02072 (1999).
- 440 12. Bukovsky, M. S. & Karoly, D. J. A regional modeling study of climate change impacts on
441 warm-season precipitation in the central United States. *J. Climate*, **24**, 1985–2002 (2011).
- 442 13. Tang, J. P., et al. Building Asian climate change scenario by multiregional climate models
443 ensemble. Part I: Surface air temperature. *Int. J. Climatol.*, **36**, 4241–4252 (2016).
- 444 14. Wu, W. & Lynch, A. H. Response of the seasonal carbon cycle in high latitudes to climate
445 anomalies. *J. Geophys. Res.* **105 (D18)**, 22897–22908 (2000).
- 446 15. Sato, T., Kimura, F. & Kitoh, A. Projection of global warming onto regional precipitation
447 over Mongolia using a regional climate model. *J. Hydrol.*, **333**, 144–154 (2007).
- 448 16. Xu, Z. F. & Yang, Z.-L. An Improved Dynamical Downscaling Method with GCM Bias
449 Corrections and Its Validation with 30 Years of Climate Simulations. *J. Climate*, **25**, 6271–
450 6286 (2012).
- 451 17. Holland, G. J., Done, J., Bruyere, C., Cooper, C. & Suzuki, A. Model investigations of the
452 effects of climate variability and change on future Gulf of Mexico tropical cyclone activity.
453 Proc. Offshore Technology Conf., Houston, TX, ASCE, OTC 20690, (2010).
- 454 18. Done, J. M., Holland, G. J., Bruyère, C. L., Leung, L. R. & Suzuki-Parker, A. Modeling high-
455 impact weather and climate: Lessons from a tropical cyclone perspective. *Clim. Change*,
456 **129**, 381–395 (2015).
- 457 19. Bruyère, C. L., Done, J. M., Holland, G. J. & Fredrick, S. Bias corrections of global models
458 for regional climate simulations of high-impact weather. *Clim. Dyn.*, **43**, 1847–1856 (2014).
- 459 20. Xu, Z. F. & Yang, Z.-L.: A new dynamical downscaling approach with GCM bias corrections
460 and spectral nudging. *J. Geophys. Res. Atmos.*, doi:10.1002/2014JD022958 (2015).
- 461 21. Colette, A., Vautard, R. & Vrac M. Regional climate downscaling with prior statistical
462 correction of the global climate forcing. *Geophys. Res. Lett.*, **39**, L13707 (2012).

- 463 22. Rocheta, E., Evans, J. P. & Sharma, A. Can Bias Correction of Regional Climate Model
464 Lateral Boundary Conditions Improve Low-Frequency Rainfall Variability? *J. Clim.*, **30**,
465 9785–9806 (2017).
- 466 23. Dai, A. G., Rasmussen, R. M., Ikeda, K. & Liu, C. H. A new approach to construct
467 representative future forcing data for dynamic downscaling. *Clim. Dyn.*, doi:
468 10.1007/s00382-017-3708-8 (2017).
- 469 24. Xu, Z. F., Han, Y. & Yang, Z.-L.: Dynamical downscaling of regional climate: A review of
470 methods and limitations. *Science China Earth Sciences*, **129**.
471 <https://doi.org/10.1007/s11430-018-9261-5> (2019).
- 472 25. Adachi, S. A. & Tomita, H. Methodology of the constraint condition in dynamical
473 downscaling for regional climate evaluation: A review. *J. Geophys. Res. Atmos.*, **125(11)**,
474 DOI:10.1029/2019JD032166 (2020).
- 475 26. White, R. H. & Toumi, R. The limitations of bias correcting regional climate model inputs.
476 *Geophys. Res. Lett.*, **40**, 2907–2912, doi:10.1002/grl.50612 (2013).
- 477 27. IPCC. Climate Change 2013. The Physical Science Basis. Contribution of Working Group I
478 to the Fifth Assessment Report of the Intergovernmental Panel on Climate Change. In:
479 Stocker T F, Qin D, Plattner G K, Tignor M, Allen S K, Boschung J, Nauels A, Xia Y, Bex V,
480 Midgley P M, eds. Cambridge: Cambridge University Press. 1535 (2013).
- 481 28. Latif, M. Uncertainty in climate change projections. *Journal of Geochemical Exploration*,
482 **110**, 1–7, (2011).
- 483 29. Eyring, V. et al. Overview of the Coupled Model Intercomparison Project Phase 6 (CMIP6)
484 experimental design and organization. *Geoscientific Model Development*, **9(5)**, 1937–1958.
485 <https://doi.org/10.5194/gmd-9-1937-2016> (2016).
- 486 30. Huang, F., Xu, Z., Guo, W.: Evaluating vector winds in the Asian-Australian monsoon
487 region simulated by 37 CMIP5 models. *Clim. Dyn.*, **53**: 491.
488 <https://doi.org/10.1007/s00382-018-4599-z>, 2019.
- 489 31. Richter, I. & Tokinaga, H. An overview of the performance of CMIP6 models in the tropical
490 Atlantic: mean state, variability, and remote impacts. *Clim. Dyn.*, **55**, 2579–2601 (2020).
- 491 32. Mauritsen, T., et al. Developments in the MPI-M Earth System Model version 1.2 (MPI-
492 ESM1.2) and its response to increasing CO₂. *Journal of Advances in Modeling Earth*
493 *Systems*, **11**, 998–1038 (2019).
- 494 33. Müller, W. A., et al.: A high-resolution version of the Max Planck Institute Earth System
495 Model MPI-ESM1.2-HR. *Journal of Advances in Modeling Earth Systems*, **10**, 1383–1413
496 (2018).
- 497 34. Krümer, T. R., Giorgetta, M. A. & Esch, M.: Seasonal aspects of the quasi-biennial
498 oscillation in MPI-ESM and ERA-40. *Journal of Advances in Modeling Earth Systems*, **5**,
499 406–421, <https://doi.org/10.1002/jame.20024> (2013).
- 500 35. Hersbach, H., et al. The ERA5 global reanalysis. *Quarterly Journal of the Royal*
501 *Meteorological Society*, **146**, 1999–2049 (2020).
- 502 36. Wu, Z. & Huang, N. E. Ensemble Empirical Mode Decomposition: a noise-assisted data
503 analysis method. *Advances in Adaptive Data Analysis*, **1**, 1–41 (2009).
- 504 37. Hoffmann, P., Katzfey, J. J., McGregor, J. L. & Thatcher, M. Bias and variance correction of
505 sea surface temperatures used for dynamical downscaling, *J. Geophys. Res. Atmos.*, **121**,
506 doi:10.1002/2016JD025383 (2016).
- 507 38. Xu, Z. F., Hou, Z. L., Han, Y. & Guo, W. D.: A diagram for evaluating multiple aspects of
508 model performance in simulating vector fields, *Geosci. Model Dev.*, doi:10.5194/gmd-
509 2016-172, (2016).
- 510 39. Xu, Z. F., Han, Y. & Fu, C.: Multivariable Integrated Evaluation of Model Performance with
511 the Vector Field Evaluation Diagram. *Geosci. Model Dev.*, **10**, 3805–3820,
512 <https://doi.org/10.5194/gmd-10-3805-2017> (2017).

- 513 40.Zhang, M.-Z., Xu, Z. F., Han, Y. & Guo, W. D. An improved multivariable integrated
514 evaluation method and NCL code for multimodel intercomparison. *Geosci. Model Dev.*
515 *Diss.* <https://gmd.copernicus.org/preprints/gmd-2020-310/> (2020).
- 516 41.Xu, Z. F. Bias-corrected CMIP6 global dataset for dynamical downscaling of future climate,
517 1979-2100. V1. China Science Data
518 Bank. <http://www.dx.doi.org/10.11922/sciencedb.00487> (2021).
- 519 42.Rocheta, E., Evans, J. P. & Sharma, A. Correcting lateral boundary biases in regional
520 climate modeling – the effect of the relaxation zone. *Clim. Dyn.*
521 <https://doi.org/10.1007/s00382-020-05393-1> (2020).
- 522 43.Huang, F., Xu, Z., Guo, W. The linkage between CMIP5 climate models’ abilities to
523 simulate precipitation and vector winds. *Clim. Dyn.*, **54**, 4953–4970 (2020).
- 524 44.Meyer, J. D. D. & Jin, J. M. Bias correction of the CCSM4 for improved regional climate
525 modeling of the North American monsoon. *Clim. Dyn.*, **46**, 2961–2976 (2015).

Figures

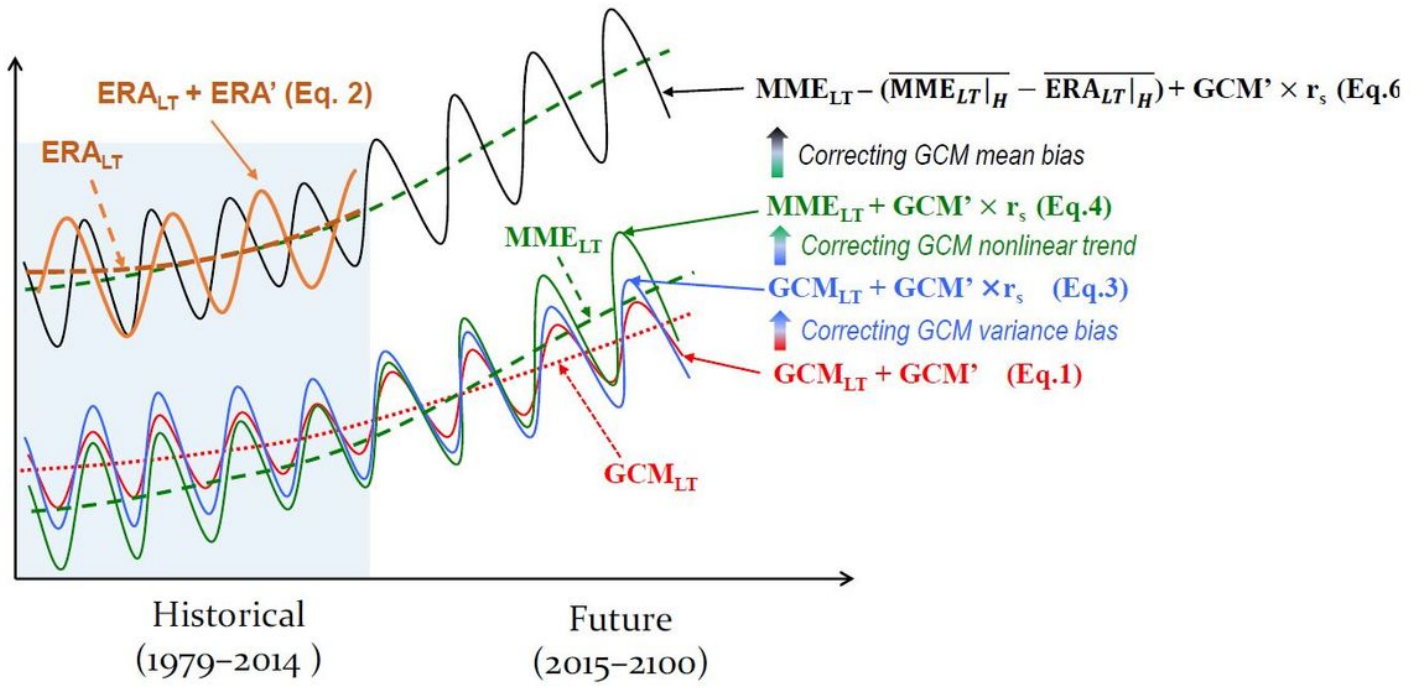


Figure 1

Schematic chart for the process of GCM bias corrections

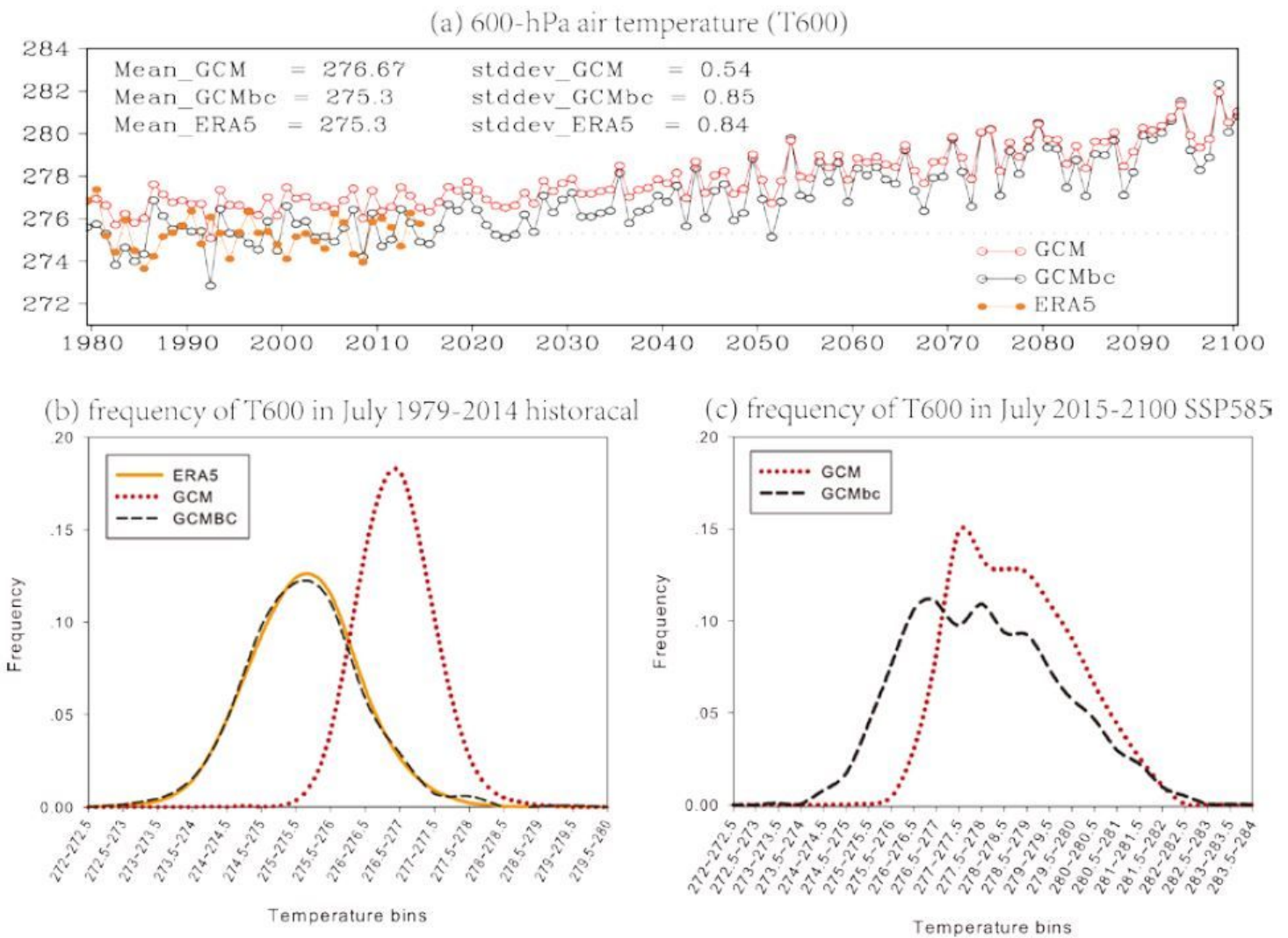


Figure 2

Comparison of the original and bias-corrected data GCM data (GCMbc) with ERA5 during the historical (1979–2014) period and SSP585 scenarios (2015–2100). (a) 600-hPa air temperature (T600) in Northwest Pacific (10°N, 135°E) at 00 UTC July 15 from 1979 to 2100. The 36-yr averaged (1979–2014) value and temporal standard deviation for each data are shown on the upper-left of (a). The frequency distribution of T600 in July during the period of (a) 1979–2014 and (b) 2015–2100 under SSP585 scenarios. The frequency (in percentage) is computed based on the instantaneous data at 00 UTC in July. There are 1116 days (31 day × 36 year) and 2666 days (31 day × 86 year) are included in the statistics for the historical and future periods, respectively.

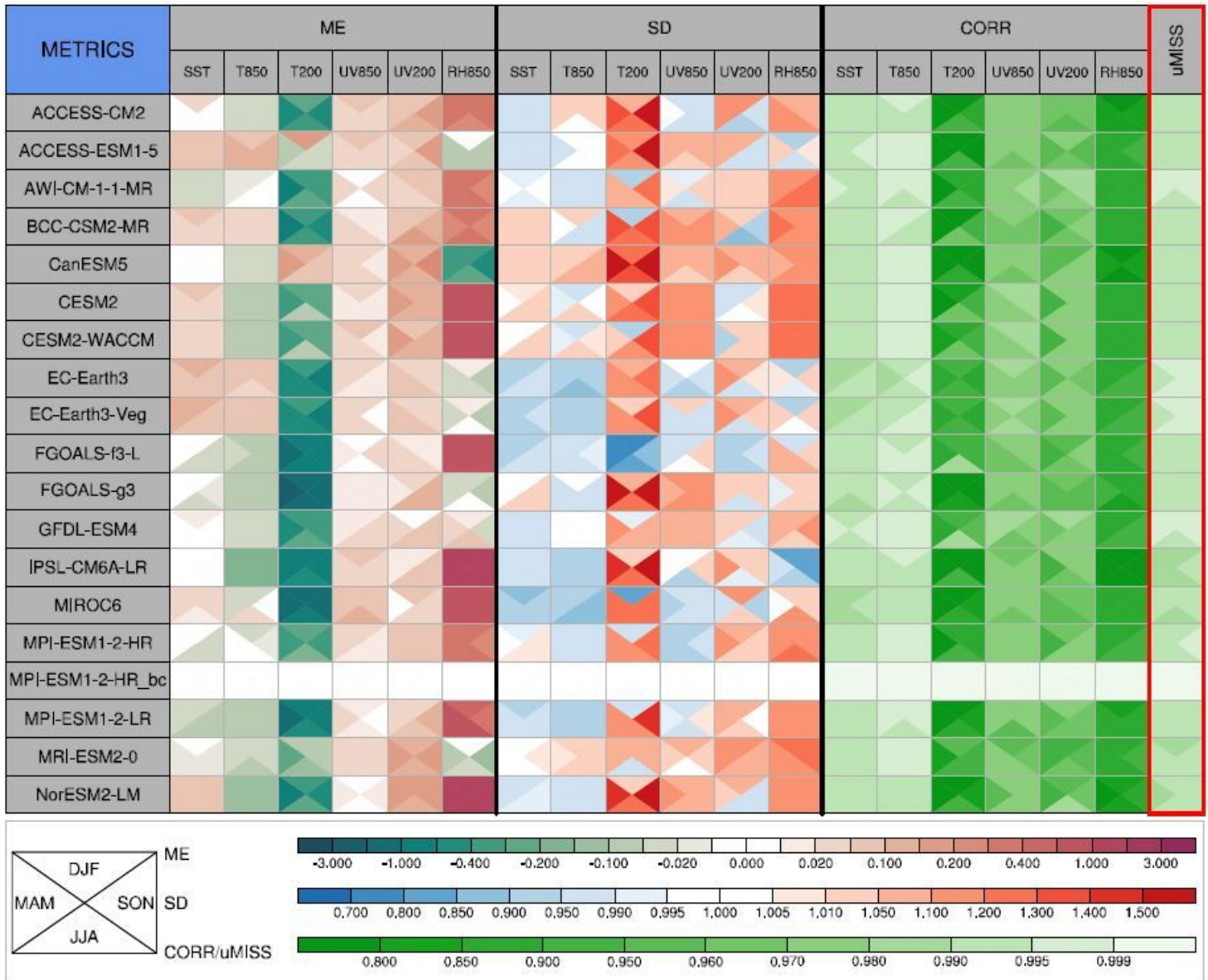


Figure 3

Statistical metrics that measure the performance of CMIP6 models in simulating climatological mean (1979 – 2014) of multiple variables. SST: sea surface temperature, T850: 850-hPa air temperature, UV850: 850-hPa vector wind, RH850: 850-hPa relative humidity, T200: 200-hPa air temperature, UV200: 200-hPa vector wind in the global. ME, SD, and CORR are the mean error, spatial standard deviation, and correlation coefficient of the climatological mean field, respectively. uMISS is the uncentered multivariable integrated skill score that summarizes the overall performance of a model in simulating multiple variables. All statistics are normalized by dividing the observed standard deviation of the corresponding variable. All models are evaluated against ERA5. Lighter color represents better model performance. MPI-ESM1-2-HR_bc is the bias-corrected GCM data.

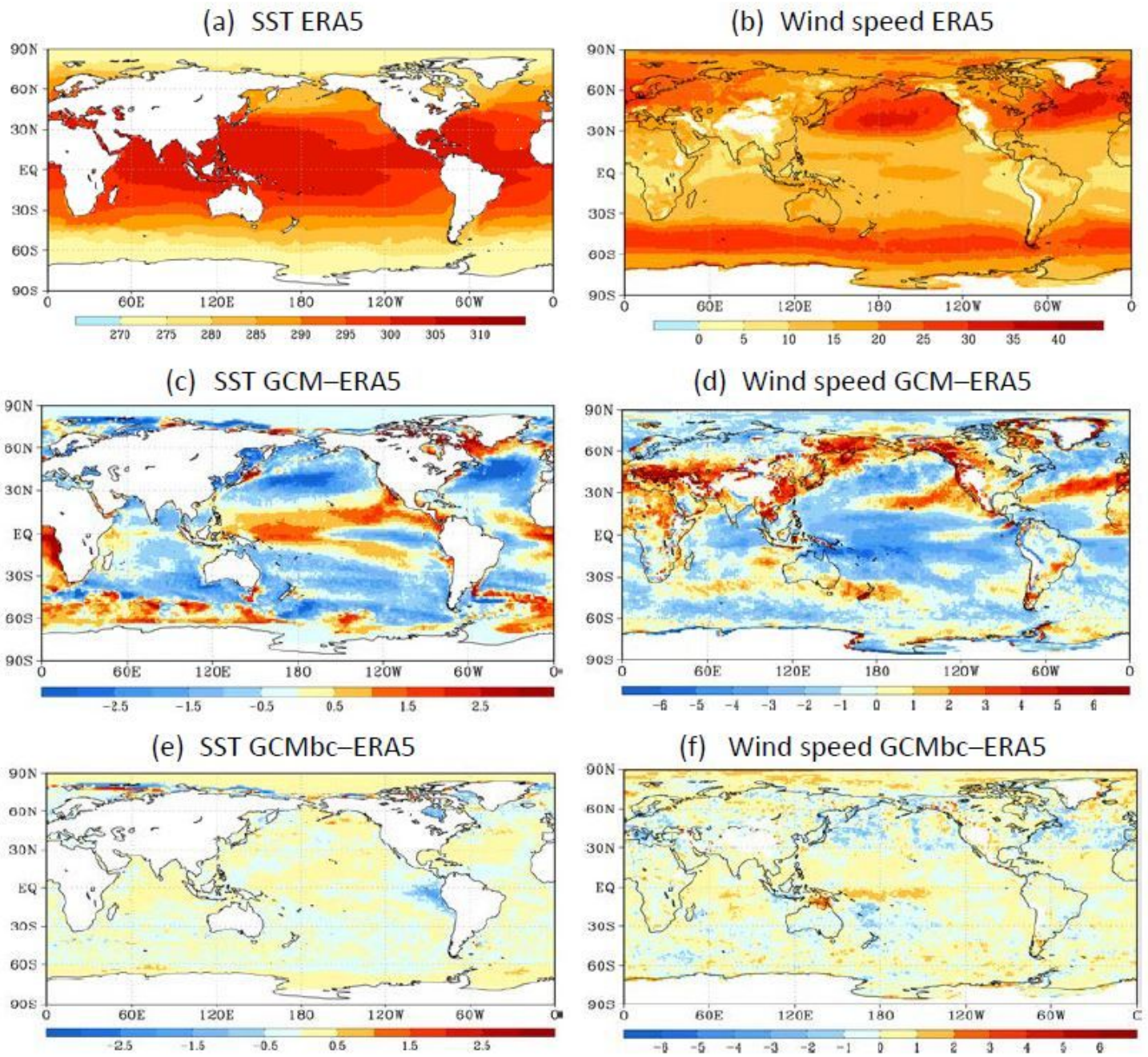
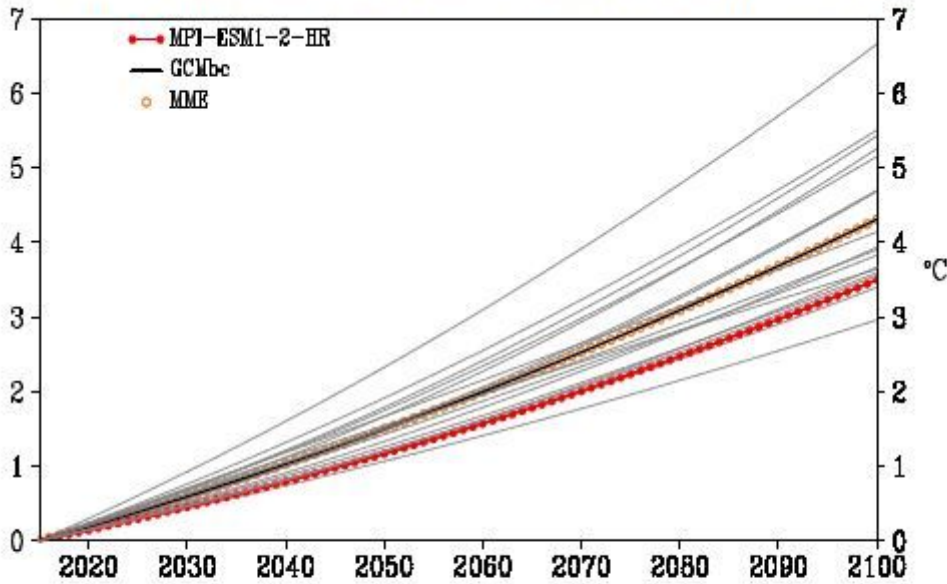


Figure 4

Comparison of the 95th percentile of daily SST ($^{\circ}\text{C}$) and 850-hPa wind speed wind (m s^{-1}) during July of 1979–2014 against ERA5. (a, b) ERA5, (c-f) difference between GCM (GCMbc) and ERA5. Note: The designations employed and the presentation of the material on this map do not imply the expression of any opinion whatsoever on the part of Research Square concerning the legal status of any country, territory, city or area or of its authorities, or concerning the delimitation of its frontiers or boundaries. This map has been provided by the authors.

(a) Nonlinear trends of 850-hPa air temperature



(b) RMSDs of nonlinear trend

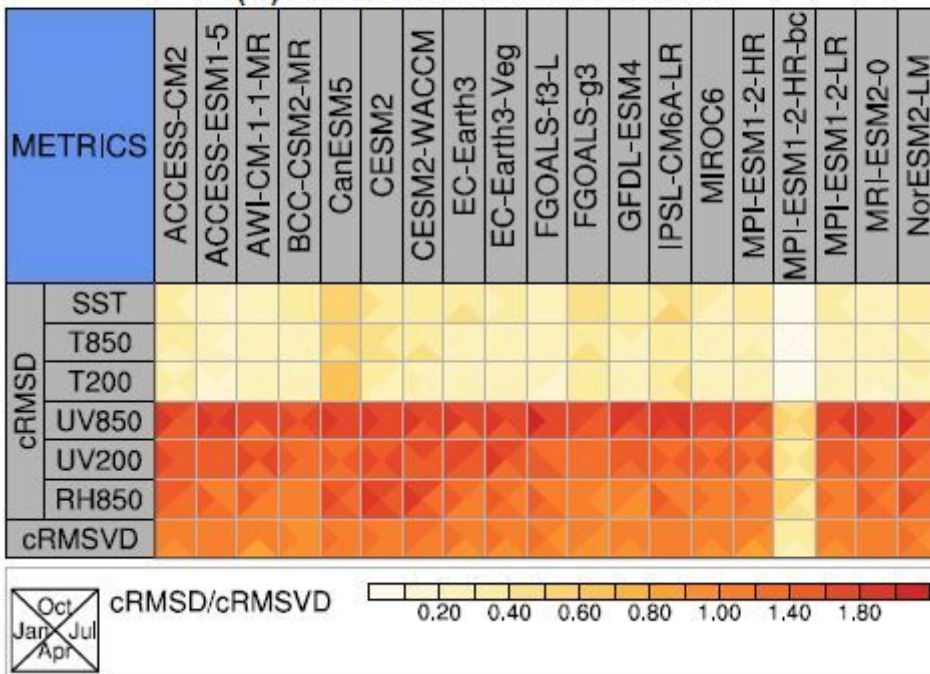


Figure 5

Comparison of Nonlinear trend of various CMIP6 data against multi-model ensemble mean (MME) in July from 2015 to 2100 under SSP585 scenario. (a) Global 850-hPa air temperature. The orange open circle, red solid circles, and the thick black line represent the MME, MPI-ESM1-2-HR model the bias-corrected MPI-ESM1-2-HR model, respectively. The grey line indicates the other 17 CMIP6 models. The value of the non-linear trend in the year 2015 was subtracted from the original non-linear trend. (b) root-mean-square differences of the non-linear trends between the individual CMIP6 model and the MME. As

in Fig. 3 the cRMSDs are also normalized by dividing the observed standard deviation of the corresponding variable. The cRMSVD represents the overall RMSD of all variables. The triangles in each grid cell represent the statistic in January, April, July, and October, respectively.

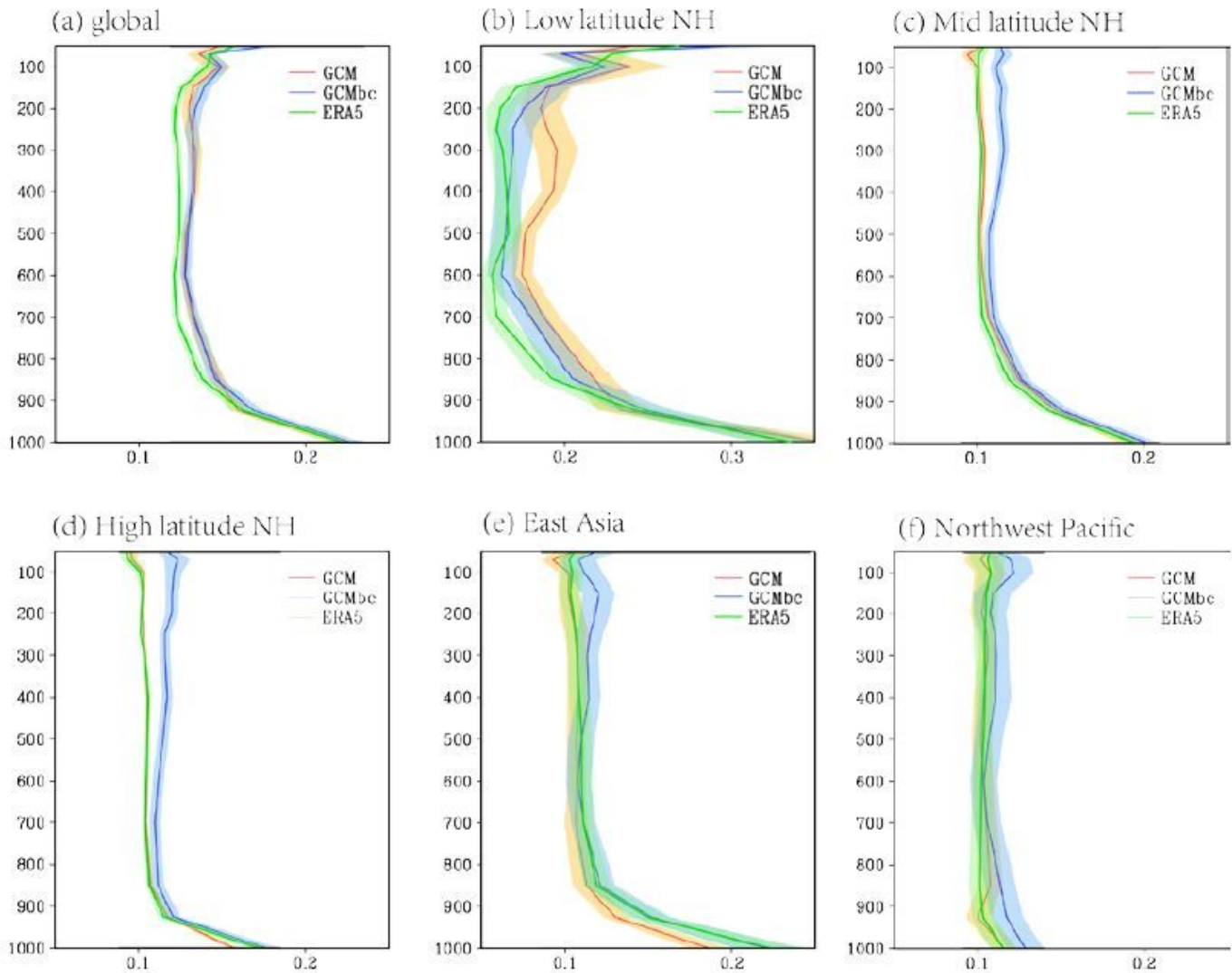


Figure 6

The ratio (R) of ageostrophic wind speed to the real wind speed averaged over various regions in July 2014. The shading shows the one standard deviation. The ageostrophic wind and real wind are calculated using 6-hourly data in July 2014. The area-mean R is computed in mid (20° – 50° N, 0 – 358.75° E) and high latitudes (50 – 90° N, 0 – 358.75° E) of Northern Hemisphere, East Asia (10° – 55° N, 105° – 140° E), and Northwest Pacific (10° – 40° N, 135° E– 180°). The grid cells with wind speed less than 2 m s^{-1} were excluded from the statistics.